Chemical Science

ROYAL SOCIETY OF CHEMISTRY

EDGE ARTICLE

View Article Online
View Journal | View Issue

Cite this: *Chem. Sci.*, 2025, **16**, 182

All publication charges for this article have been paid for by the Royal Society of Chemistry

Synergistic global and local flexibilities in Zr-based metal–organic frameworks enable sequential sieving of hexane isomers†

Rundao Chen, ‡[a] Jiaqi Li,‡[a] Fang Zheng,*[b] Fangru Zhou,[a] Bin Sheng,[a] Baojian Liu,[b] Qiwei Yang,[ab] Zhiguo Zhang,[ab] Qilong Ren[ab] and Zongbi Bao *[ab]

Received 27th August 2024
Accepted 25th October 2024

DOI: 10.1039/d4sc05749j

rsc.li/chemical-science

Separating hexane isomers based on the branching degree is crucial for their efficient utilization in the petrochemical industry, yet remains challenging due to their similar properties. Here we report a temperature-responsive Zr-based metal–organic framework, Zr-fum-FA, capable of sequentially sieving linear, mono-, and di-branched hexane isomers. Notably, the pore structure of Zr-fum-FA dynamically transforms from segmented triangular channels to an integrated rhombic configuration as the temperature increases, leading to distinct sieving effects. At low temperatures, the narrow triangular pores allow the exclusive adsorption of *n*-hexane while excluding branched isomers. In contrast, the expanded rhombic pores at high temperatures enable the sieving of mono- and di-branched isomers. Mechanistic studies reveal that this unique dual-sieving behavior originates from the synergistic effects of the global framework flexibility and the local dynamics of pendent hydroxyl groups. Furthermore, we demonstrate the decoupling of global and local flexibilities *via* two strategies: incorporating steric hindrance to dampen the global framework dynamics and enhancing the metal node rigidity to limit the local vibrations. These findings not only provide a promising adsorbent for the challenging separation of hexane isomers but also offer rational design principles for harnessing flexibility in MOFs.

Introduction

Hexane isomers, obtained as mixtures from the paraffin isomerization process,[1] play crucial roles in the petrochemical industry. The linear *n*-hexane (*n*-Hex) serves as an ideal feedstock for the ethylene cracking unit,[2] while its branched isomers, including the mono-branched 2-methylpentane (2-MP) and 3-methylpentane (3-MP), and especially di-branched 2,3-dimethylbutane (2,3-DMB) and 2,2-dimethylbutane (2,2-DMB), are critical components in high-grade clean gasoline with improved research octane number (RON).[3] Therefore, the sequential separation of hexane isomers based on their branching degrees is of great significance for their efficient and comprehensive utilization. However, this separation is severely hindered by the similar kinetic diameters and electrostatic properties of these isomers[4] (Table S1†).

Extensive efforts have been devoted to developing advanced adsorbents for the efficient adsorptive separation of hexane isomers.[5] Zeolite 5A, a well-established adsorbent, can sieve *n*-Hex from other isomers with larger kinetic diameters.[6] Benefitting from their highly designable and controllable pore structures and sizes,[7–15] metal–organic frameworks (MOFs) have been constructed for the sieving of *n*-Hex from branched isomers,[16–20] and even the further sieving of mono- and di-branched hexane isomers.[21–30] However, the fixed pore structure of both zeolites and rigid MOFs results in a sole point of clean cut among varied isomers, while the residual components can only be separated based on their subtle thermodynamic[31–35] or kinetic[36–40] differences on these rigid-pore adsorbents.

To achieve the synergistical clean sieving of the three types of hexane isomers according to their branching degrees on a single adsorbent, structural flexibility is an essential consideration.[41] The pore structures of dynamic adsorbents can automatically switch to accommodate different isomers under various separation conditions. Ca-tcpb[42] is a pioneering example of flexible MOFs with two clean cut points for sieving hexane isomers at different temperatures, followed by HIAM-203,[43] Mn-dhbq,[44] CopzNi,[45] *etc.* However, the origin and precise

[a]*Key Laboratory of Biomass Chemical Engineering of the Ministry of Education, College of Chemical and Biological Engineering, Zhejiang University, 866 Yuhangtang Road, Hangzhou 310058, China. E-mail: baozb@zju.edu.cn*

[b]*Institute of Zhejiang University-Quzhou, Zhejiang University, 99 Zheda Road, Quzhou 324000, China. E-mail: zhengfang_@zju.edu.cn*

† Electronic supplementary information (ESI) available: Experimental procedures, Rietveld refinements, N_2 adsorption–desorption isotherms at 77 K, TG curves, hexane isomer isotherms, calculations of isosteric heats and kinetics, breakthrough curves, stability tests, *in situ* PXRD and DRIFTS patterns, physical properties of hexane isomers, crystallographic data, hexane isomer adsorption capacity comparison with other materials, heats of adsorption, mass-transfer coefficients, and DFT calculated energies. See DOI: https://doi.org/10.1039/d4sc05749j

‡ R. Chen and J. Li contributed equally to this work.

control of the temperature-responsive flexibility in these materials remain ambiguous, hindering the further rational design of adsorbents with desired dynamic behaviors.

Herein, we present a Zr-based dynamic MOF, termed Zr-fum-FA, that exhibits structural transformation during temperature swing processes, enabling the concurrent sieving of normal, mono-, and di-branched hexane isomers. Validated by *in situ* powder X-ray diffraction (PXRD) and variable-temperature diffuse reflectance infrared Fourier transform spectroscopy (VT-DRIFTS), the temperature-responsive flexibility of the material results in regulable pore size and cross-section shape to accommodate different hexanes, and therefore the switched cut point among isomers with different branching degrees at programmed temperatures. Furthermore, drawing inspiration from the tuned mass dampers in architecture to reduce the shaking of skyscrapers, and the scaffold fasteners to enhance local robustness (Fig. 1a), the temperature-responsive flexibility of the adsorbent (Fig. 1b) has been rationally controlled and decoupled *via* two distinct strategies: damping block introduction (for Zr-mes-FA, Fig. 1c) and metal node enhancement (for Hf-fum-FA, Fig. 1d). The respective action mechanisms of these two strategies have been elucidated clearly by both experimental and theoretical methods. These two situations with decoupled global/local flexibility support the claim that the distinctive dual-sieving performance of Zr-fum-FA should be ascribed to the synergistic effect of its global and local flexibility. Besides, the sieving performance, in addition to the considerable hexane capacity and high stability, renders these materials very promising candidates for the efficient adsorptive separation of hexane isomers.

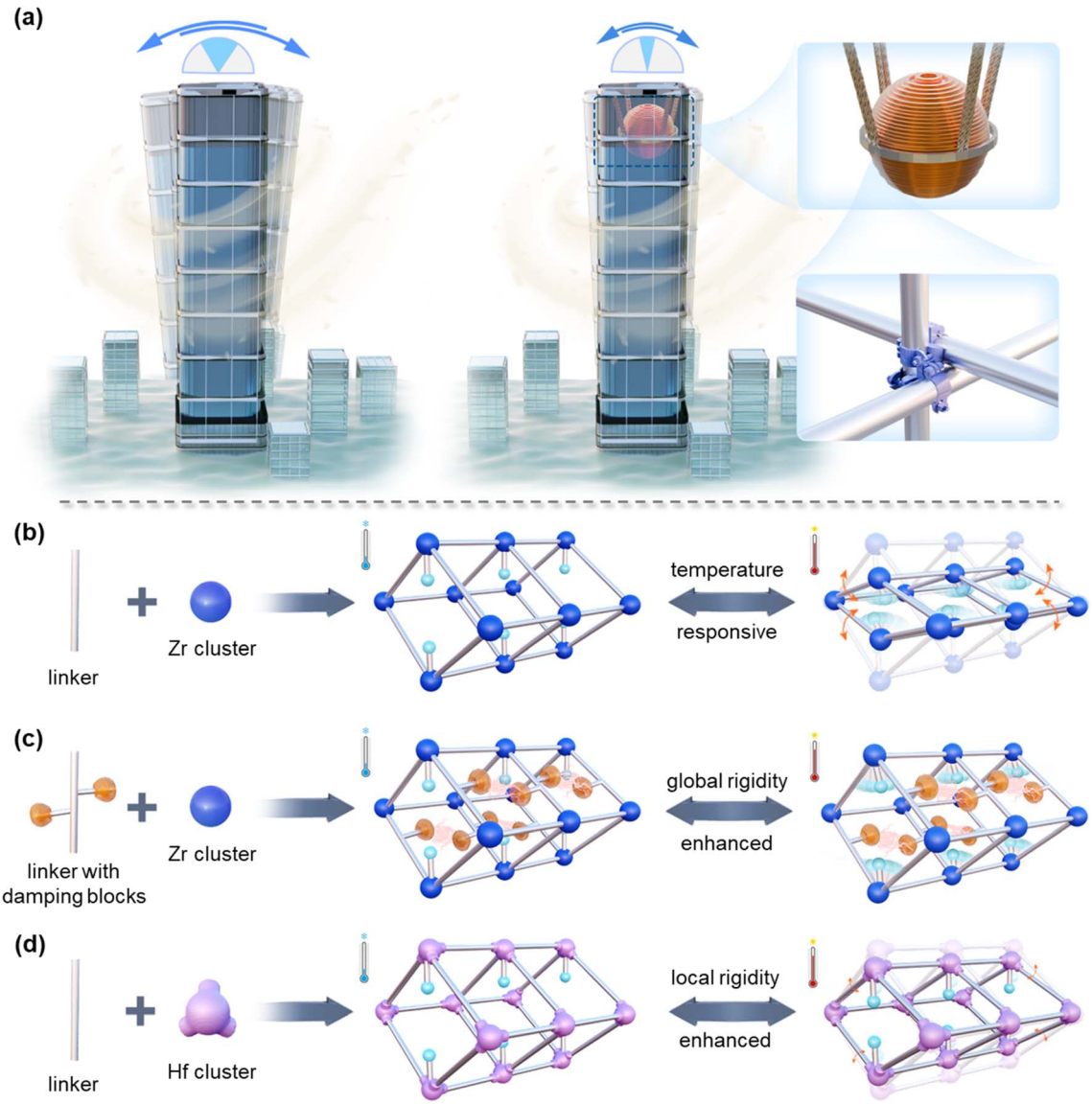

Fig. 1 Schematic illustration of flexibility control strategies. (a) The tuned mass damper of skyscrapers for reducing the overall structural vibration and scaffold fastener for enhancing the local robustness. (b) The synergism of the global dynamics and the local flexibility in the original framework. (c) Damping block introduction, and (d) metal node enhancement strategies for regulating and decoupling the global and local flexibility. The aqua and orange balls represent hydroxyl and methyl groups respectively.

Results and discussion

Characterization of materials

Taking formic acid (FA) as the predominant solvent, the three materials, Zr-fum-FA ($Zr_6(\mu_3\text{-}O)_4(\mu_3\text{-}OH)_4(fumarate)_4(formate)_2(OH)_2(H_2O)_2$), methylated Zr-mes-FA ($Zr_6(\mu_3\text{-}O)_4(\mu_3\text{-}OH)_4(mesaconate)_4(formate)_2(OH)_2(H_2O)_2$), and metal node replaced Hf-fum-FA ($Hf_6(\mu_3\text{-}O)_4(\mu_3\text{-}OH)_4(fumarate)_4(formate)_2(OH)_2(H_2O)_2$), were conveniently synthesized by solvothermal methods. The structures of the three isoreticular materials were determined using the Rietveld refinement of powder X-ray diffraction data (Fig. S1–S3†). The initial structures were modified from the published structure of MIP-203-F.[46] The refinement results indicate all three materials crystallize in the orthorhombic space group of *Immm*, with lattice parameters of $a = 10.03$ Å, $b = 12.18$ Å, $c = 19.71$ Å ($R_p = 4.10\%$, $R_{wp} = 5.19\%$, $S = 1.654$) for Zr-fum-FA, $a = 10.05$ Å, $b = 12.34$ Å, $c = 19.64$ Å ($R_p = 4.81\%$, $R_{wp} = 6.27\%$, $S = 1.998$) for Zr-mes-FA, and $a = 9.98$ Å, $b = 12.12$ Å, $c = 19.67$ Å ($R_p = 3.45\%$, $R_{wp} = 4.42\%$, $S = 1.533$) for Hf-fum-FA, respectively. The detailed structural information is listed in Tables S2–S5.† As shown in Fig. 2, the Zr_6/Hf_6-oxo clusters were diagonally connected to eight adjacent clusters through eight fumarate or mesaconate ligands, and the parallel clusters along the *a*-axis were further interlinked *via* double-formate bridges, resulting in the formation of framework structures with one-dimensional channels. Each of the methyl groups on Zr-mes-FA and the –CH groups of formates had an occupancy of 0.5. The rhombic channels were further divided into dual triangular channels by the pendent –OH groups. These triangular channels possess the pore limiting diameters (PLD) of 3.74, 3.02, and 3.73 Å and the largest cavity diameter (LCD) of 5.49, 5.29, and 5.42 Å for Zr-fum-FA, Zr-mes-FA, and Hf-fum-FA, respectively, according to the Zeo++ simulations.

The permanent porosity of the three materials was successfully validated *via* N_2 adsorption–desorption isotherms at 77 K (Fig. S4–S6†). The isoreticular structures of the three materials result in their comparable Brunauer–Emmett–Teller (BET) surface areas and pore volumes. Specifically, the BET areas were calculated to be 785, 643, and 884 $m^2\ cm^{-3}$ (440, 351, and 348 $m^2\ g^{-1}$) for Zr-fum-FA, Zr-mes-FA, and Hf-fum-FA, and the total pore volumes at $P/P_0 = 0.95$ were 0.330, 0.253, and 0.356 $cm^3\ cm^{-3}$ (0.185, 0.138, and 0.140 $cm^3\ g^{-1}$), respectively. The relatively lower surface area and porosity of Zr-mes-FA can be attributed to the steric hindrance caused by the presence of methyl groups. Moreover, the steep isotherms indicated the presence of ultramicropores in all three materials. This was further confirmed by the Horvath–Kawazoe (H–K) pore size distribution curves (Fig. S4–S6†). The H–K peak pore widths of Zr-fum-FA, Zr-mes-FA, and Hf-fum-FA were found to be 5.1, 4.9, and 4.9 Å, respectively, which matched well with their corresponding framework structures. Additionally, the

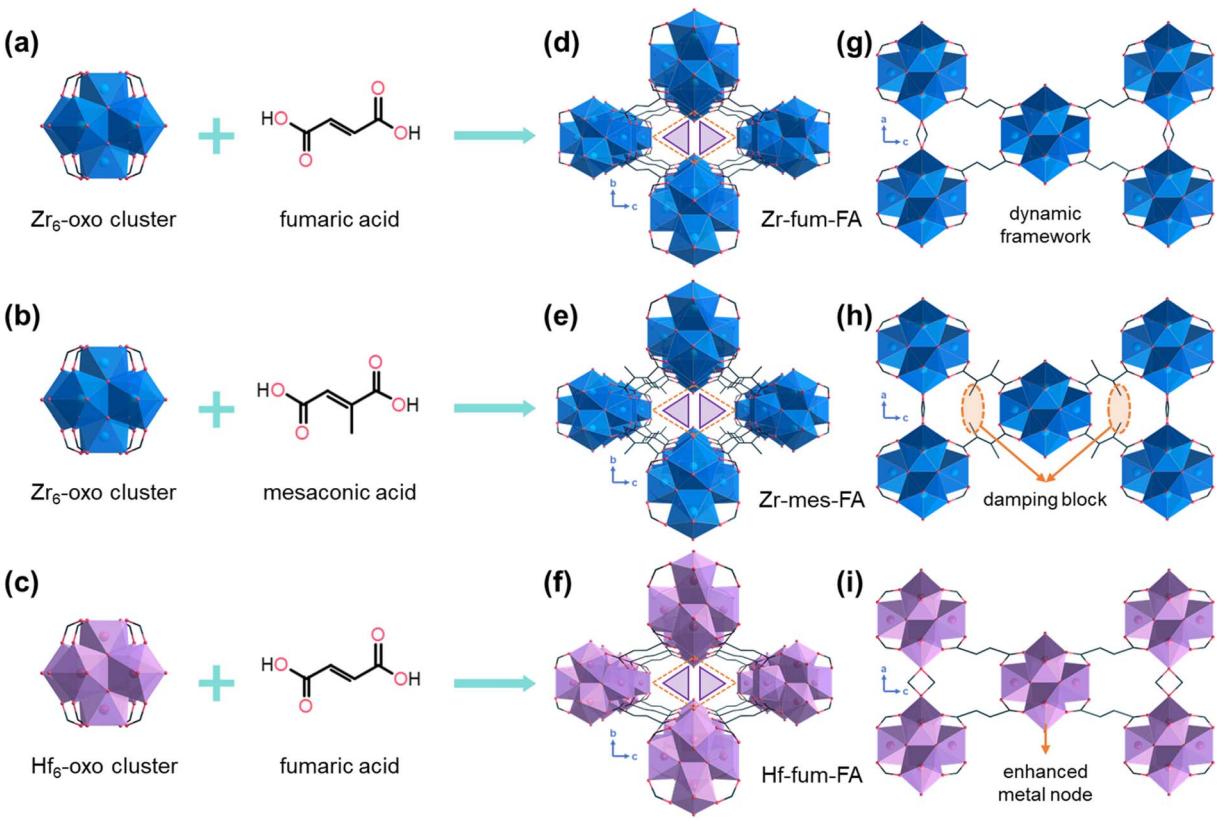

Fig. 2 Component and structure of the three materials. The metal clusters and organic ligands of (a) Zr-fum-FA, (b) Zr-mes-FA, and (c) Hf-fum-FA. (d–f) The double triangle 1D pores along *a*-axes and (g–i) the corresponding vertical view along *b*-axes of the three materials respectively. Each of the methyl groups on Zr-mes-FA and the –CH groups of formate have an occupancy of 0.5. Color scheme: black: C, red: O, blue: Zr, pink: Hf. H atoms are omitted for clarity.

thermogravimetric (TG) curves of Zr-fum-FA, Zr-mes-FA, and Hf-fum-FA (Fig. S7†) indicated their good thermal stability, as all three materials remain intact below 473 K.

Single-component adsorption

The single-component vapor isotherms of hexane isomers on Zr-fum-FA, Zr-mes-FA, and Hf-fum-FA were measured up to 20 kPa from 303 K to 423 K (Fig. 3a–c, and S8–S22†). At 303 K, all three materials exhibited similar adsorption characteristics towards hexane isomers. Specifically, the materials were capable of adsorbing *n*-Hex strongly with considerable capacities of 2.40, 2.00, and 1.41 mmol cm^{-3} at 10 kPa for Hf-fum-FA, Zr-fum-FA, and Zr-mes-FA, respectively. These values represented some of the highest reported adsorption capacities for hexane isomer separation (Fig. 3d, and Table S6†). In contrast, the adsorption of mono-branched 2-MP and 3-MP was significantly suppressed due to their incompatible molecular shape and size with the triangular micropores of the materials. Furthermore, the most bulky di-branched 2,3-DMB and 2,2-DMB were totally excluded by all three materials. Consequently, the uptake ratios of *n*-Hex over the branched isomers were considerably high among all adsorbents (Fig. 3d).

Surprisingly, with increasing temperature, divergent adsorptive behaviors have been observed on the three isoreticular materials. In the case of Zr-fum-FA, the adsorption of mono-branched isomers was maintained or even enhanced under higher temperatures, which can be attributed to the improved mass-transfer kinetics. The 3-MP capacities at 10 kPa were 0.58, 0.55, 0.72, 0.93, and 0.88 mmol cm^{-3}, at 303, 333, 363, 393, and 423 K, respectively. Conversely, the preferred adsorption of *n*-Hex and size exclusion of di-branched isomers are negligibly influenced by the temperature variations, resulting in a switched clear separation between mono- and di-branched isomers at 423 K, as illustrated in Fig. 3b. On the other hand, most of the adsorption ability of Zr-mes-FA was lost at 423 K for all five hexane isomers (Fig. 3c), leaving only linear isotherms with sharply reduced capacities. The affinity of hexane isomers on Hf-fum-FA also decreased dramatically, while the capacities were partially maintained, benefiting from its higher porosity than Zr-mes-FA.

The isosteric heats of adsorption for linear and mono-branched isomers on the three materials were further calculated with the Clausius–Clapeyron equation and also measured by the differential scanning calorimetry (DSC) method (Fig. 3e, and Table S7†). The calculation results (Fig. S23†) demonstrated that all three materials exhibit higher Q_{st} values towards *n*-Hex (−40.9, −53.9 and −37.2 kJ mol^{-1} on Zr-fum-FA, Zr-mes-FA, and Hf-fum-FA, respectively) compared to the mono-branched isomers (−28.8, −36.6, and −27.5 kJ mol^{-1} for 3-MP, −27.3, −36.1, and −25.9 kJ mol^{-1} for 2-MP), which aligns well with the DSC measurements conducted on Zr-fum-FA (−39.2, −22.9, and −15.9 kJ mol^{-1} for *n*-Hex, 3-MP, and 2-MP, respectively, Fig. S24–S26†). Moreover, the isosteric heats of all three isomers on Zr-mes-FA were found to be higher than those on Zr-fum-FA and Hf-fum-FA, which can be attributed to the stronger dispersion interactions provided by the methyl groups and the more compact pore structure.

The time-dependent adsorption amounts of *n*-Hex on the three materials (Fig. S27–S29†) have been recorded during isotherm tests, and fitted with the linear driving force (LDF) model[47] to derive the mass-transfer coefficients. As summarized in Table S8,† the diffusion kinetics were significantly enhanced

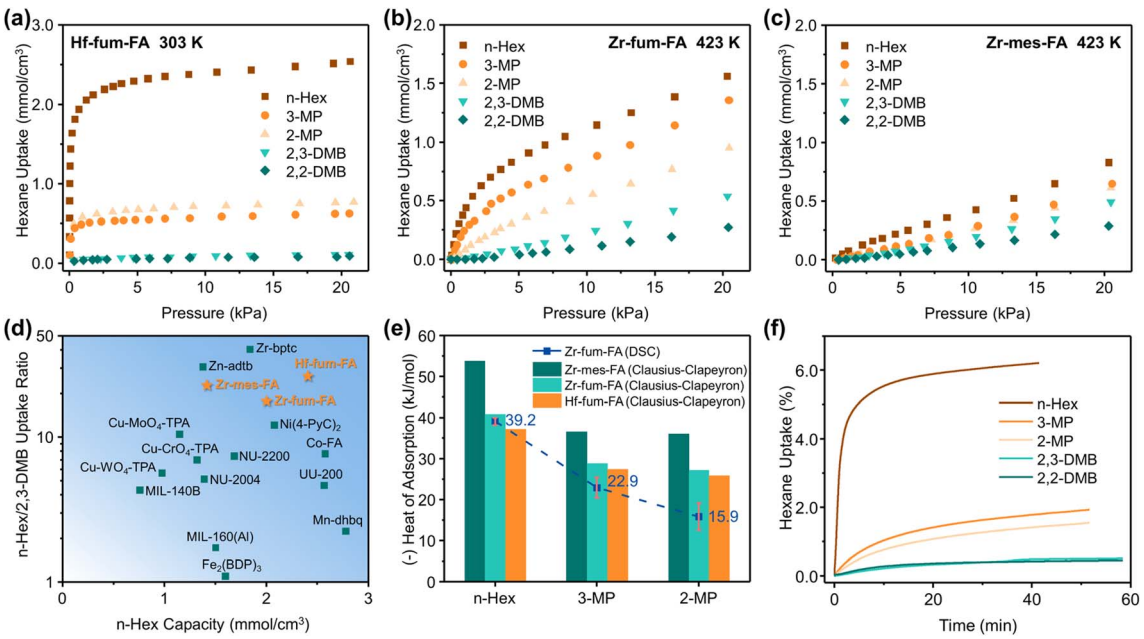

Fig. 3 Single-component hexane isomer adsorption on the three materials. Hexane isomer isotherms on (a) Hf-fum-FA at 303 K, (b) Zr-fum-FA at 423 K, and (c) Zr-mes-FA at 423 K. (d) Separation performance comparison among Zr-fum-FA, Zr-mes-FA, Hf-fum-FA, and other materials at 303 K, 10 kPa. (e) Calculated and DSC-derived heats of adsorption of hexane isomers on the three materials, the error bars represent the standard error. (f) Adsorption kinetics of hexane isomers on Zr-fum-FA at 303 K, 15 kPa.

above 363 K, and an obvious deviation from the linear relationship described by the Arrhenius equation was observed in the $\ln K - 1/T$ plot (Fig. S30†), indicating the presence of varied diffusion pathways of *n*-Hex on the three materials at different temperatures. Taking the mass-transfer coefficients at 363, 393, and 423 K for the linear fitting, the activation energies of diffusion were calculated to be 53.1, 63.6, and 48.4 kJ mol^{-1} for *n*-Hex on Zr-fum-FA, Zr-mes-FA, and Hf-fum-FA, respectively. In addition to the volumetric experiments, the adsorption kinetics of different hexane isomers on Zr-fum-FA have also been measured using the gravimetric apparatus (Fig. 3f), confirming the significantly faster diffusion of *n*-Hex than other isomers on the material, and especially the complete exclusion of di-branched ones.

Column breakthrough and cycling experiments

In light of the thermodynamic and kinetic discrepancies observed during the single-component adsorption, binary and quinary vapor breakthrough experiments were conducted to assess the overall separation performance of the three materials. In the temperature range from 303 to 423 K, Zr-fum-FA demonstrated a remarkable capability to effectively separate *n*-Hex/3-MP. This was evident from the binary equimolar breakthrough curves (Fig. S31–S35†), wherein Zr-fum-FA exhibited a comprehensive selectivity of 5.7 at 303 K and 2.8 even at 423 K. It is noteworthy that the breakthrough time for 3-MP increased dramatically from 303 to 363 K (40, 56, and 72 min, at 303, 333, and 363 K, respectively), and remained almost unchanged at higher temperatures (70 and 62 min at 393 and 423 K), indicating that the adsorption of 3-MP on Zr-fum-FA was primarily governed by kinetics, and thus enhanced at elevated temperatures.

Therefore, further breakthrough tests were conducted to verify this claim using the equimolar mixture of 3-MP and 2,3-DMB. The breakthrough curves (Fig. 4a, and S36-S40†) indicated that 2,3-DMB can hardly enter the pores of Zr-fum-FA. The adsorption of 3-MP at low temperatures was also severely restricted by slow diffusion kinetics, resulting in its apparent exclusion and immediate elution from the column. Thus the 3-MP/2,3-DMB breakthrough selectivity is only 2.2 at 303 K. However, at higher temperatures, the diffusion and adsorption of 3-MP were significantly enhanced, while 2,3-DMB was still excluded by the material, leading to improved separation performance of Zr-fum-FA among mono- and di-branched hexane isomers (Fig. S41†). The 3-MP/2,3-DMB selectivities were 10.3, 20.2, and 5.8 at 333, 363, and 393 K, with the longest elution time of 52 min for 3-MP at 393 K, and an average 3-MP dynamic capacity of 8.2 cm^3 cm^{-3} (Fig. 4b).

Furthermore, quinary breakthrough curves were also obtained for the three materials, as shown in Fig. 4c–d, and S42–S57.† Due to the limitations of mass-transfer kinetics and the lower partial pressure of each component in the quinary mixture, the adsorption amounts of mono-branched isomers were found to be negligible at temperatures of 303, 333, and 363 K for all three materials (Fig. 4c, and S42–S50†). Consequently, the approximate exclusion of all four branched isomers and the distinct separation of *n*-Hex from other isomers have been successfully achieved on these materials. The *n*-Hex elution time of over 60 min was observed for all situations except Zr-mes-FA at 363 K (36 min). The further increase in temperature led to distinct impacts on the separation performance of the three isoreticular materials. In the case of Zr-fum-FA, similar to

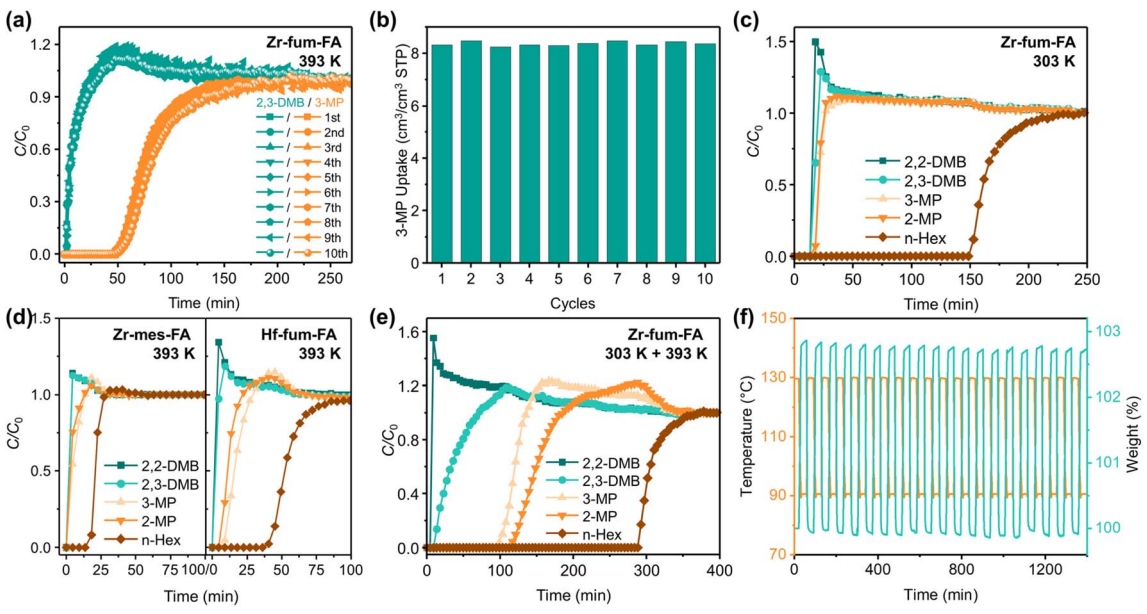

Fig. 4 Column breakthrough and cycling experiments. (a) Equimolar binary breakthrough curves of 3-MP/2,3-DMB at 393 K (10 cycles) on a column packed with Zr-fum-FA, and (b) the corresponding 3-MP uptake amounts during 10 cycles. Equimolar quinary breakthrough curves (c) on the same Zr-fum-FA column at 303 K, (d) on Zr-mes-FA (left) and Hf-fum-FA (right) columns at 393 K, and (e) on a sequence of two Zr-fum-FA columns at 303 and 393 K. (f) 20 Adsorption–desorption cycles of *n*-Hex on Zr-fum-FA among a temperature range of 363 to 403 K.

the results obtained from the binary tests, the separation of mono- and di-branched isomers can be achieved at 393, 423, or even 453 K (Fig. S51, S54, and S57†). This can be attributed to both the maintained thermodynamic affinity and the improved diffusion kinetics of linear and mono-branched isomers on the material simultaneously, indicating the happening of structural transformations during the increase of temperature. In contrast, for Zr-mes-FA, the adsorption ability weakened rapidly as temperatures rise, resulting in negligible elution times for all hexane isomers on the material at 393 and 423 K (Fig. 4d, left, S52 and S55†). Meanwhile, Hf-fum-FA exhibited an intermediate performance between Zr-fum-FA and Zr-mes-FA (Fig. 4d, right, S53 and S56†).

The temperature-responsive separation performance of Zr-fum-FA was further demonstrated through a sequential experiment conducted on two analogous Zr-fum-FA packed columns at temperatures of 303 and 393 K, respectively. Although the highest 3-MP/2,3-DMB binary selectivity appears at 363 K (Fig. S41†), a slightly elevated temperature of 393 K promotes improved diffusion rates and longer elution time for 3-MP. Therefore, as depicted in Fig. 4e, all five hexane isomers were effectively separated into three distinct fractions based on their branching degrees. The elution times are 5, 9, 99, 117, and 293 min for 2,2-DMB, 2,3-DMB, 2-MP, 3-MP, and *n*-Hex, respectively. Even in the liquid phase, the dual sieving ability of Zr-fum-FA towards hexane isomers was also maintained (Fig. S58†).

Besides, the stability of the material was assessed through 10-cycle breakthrough tests on a single packed column, which showed almost identical breakthrough times (Fig. 4a and S59†) and 3-MP uptake amounts (Fig. 4b), indicating satisfactory stability of the material. In addition to the breakthrough cycling tests, 20 adsorption–desorption cycles on Zr-fum-FA at 363/403 K with almost unchanged capacities (Fig. 4f) also validated the gratifying cyclability of the material. Besides, after all the hexane isomer vapor adsorption tests (25 cycles total), both the PXRD patterns (Fig. S60†) and N_2 adsorption–desorption isotherms at 77 K (Fig. S61 and Table S9†) of the three materials showed only a negligible loss compared with the as-synthesized samples, which implied the practical application prospect of the three materials.

Structural transformation and adsorption mechanism

The distinct temperature-responsive hexane adsorption behaviors of the three isoreticular materials were thoroughly investigated through a combination of *in situ* PXRD, DRIFTS, and first-principles density functional theory (DFT) calculation methods. As shown in Fig. 5a, the overall framework structure of Zr-fum-FA experienced two distinct stages of transformation during the temperature ramping process with the presence of bulky 3-MP. From 303 to 363 K, a noticeable right shift was observed in the (011) peaks, indicating a contraction of the interplanar spacing of (011) planes from 10.23 to 10.06 Å, while the (002) interplanar spacing exhibited a slight increase from 9.84 to 9.88 Å. Planes with the *a*-axis component ($h \neq 0$) changed negligibly. These changes were attributed to the contraction of the rhombic framework along the *b*-axis into a narrower form, while the pores remained divided by the pendent hydroxyl groups into dual triangular ones. Interestingly, at higher temperatures (>363 K), the narrowed framework expanded again with the (011) and (002) interplanar spacings of 10.13 and 9.84 Å at 423 K.

In DRIFTS, the enhanced and red-shifted vibration peaks of hydroxyl groups (Fig. 5b) further support the claim that the pendent hydroxyl groups were partially delocalized from the central position of the pore, experiencing more interactions with the framework atoms. Consequently, the segmented triangular pores of Zr-fum-FA were integrated into a large rhombic one to accommodate the bulky 3-MP, as shown in Fig. 1b. This deduction was consistent with the abnormally accelerated diffusion kinetics (Fig. S30†) and enhanced adsorption of 2- and 3-MP on Zr-fum-FA above 363 K.

The two-stage transformation process is illustrated in Fig. 5c, with corresponding interplanar spacing changes summarized in Fig. 5d. Furthermore, the reopening of the rhombic framework was slightly hindered when conducting the same *in situ* PXRD measurements under a pure N_2 flow without 3-MP (Fig. S62†), with a nearly unchanged (011) interplanar spacing of 10.06 Å from 363 K to 423 K, highlighting the significant roles of the guest molecules and host–guest interactions in the structural transformation of Zr-fum-FA.

It is worth noting that the improved separation performance of Zr-fum-FA towards hexane isomers was a result of the synergy between its globally dynamic framework and locally flexible functional groups. The enhanced vibration of hydroxyl groups facilitated the integration of dual triangular pores into one rhombic pore, enabling the entrance of the bulky mono-branched isomers. Meanwhile, the contracted framework provided more dispersive interactions, ensuring stable adsorption affinity for both *n*-Hex and mono-branched isomers even at elevated temperatures.

In contrast, the additional methyl groups in Zr-mes-FA, acting as damping blocks (Fig. 1a and c), significantly impeded the global dynamic behavior (framework contraction) of Zr-mes-FA (Fig. 5d and e). This resulted in inadequate thermodynamic affinity towards hexane isomers and thus negligible capacities under high temperatures, despite the similar enhanced flexibility of hydroxyl groups (Fig. S63†) compared to Zr-fum-FA. As for Hf-fum-FA, the overall framework deformation was negligibly affected by the substitution of the metal node (Fig. 5d), according to the *in situ* PXRD experiments (Fig. S64†). With temperature increasing, the (011) interplanar spacing of Hf-fum-FA undergoes notable contraction followed by expansion, while the (002) interplanar spacing exhibits the opposite trend, suggesting that the rhombic framework of Hf-fum-FA is also capable of contracting along the *b*-axis. However, the delocalization of hydroxyl groups was hindered significantly, as indicated by the position-fixed ν_{OH} vibration peaks in the DRIFTS spectra (Fig. 5f). *i.e.*, the Hf-substituted metal node improved the local robustness and attenuated the local flexibility, similar with the scaffold fastener (Fig. 1a). Therefore, the narrow pores of Hf-fum-FA at high temperatures were still divided and blocked by hydroxyl groups (Fig. 1d),

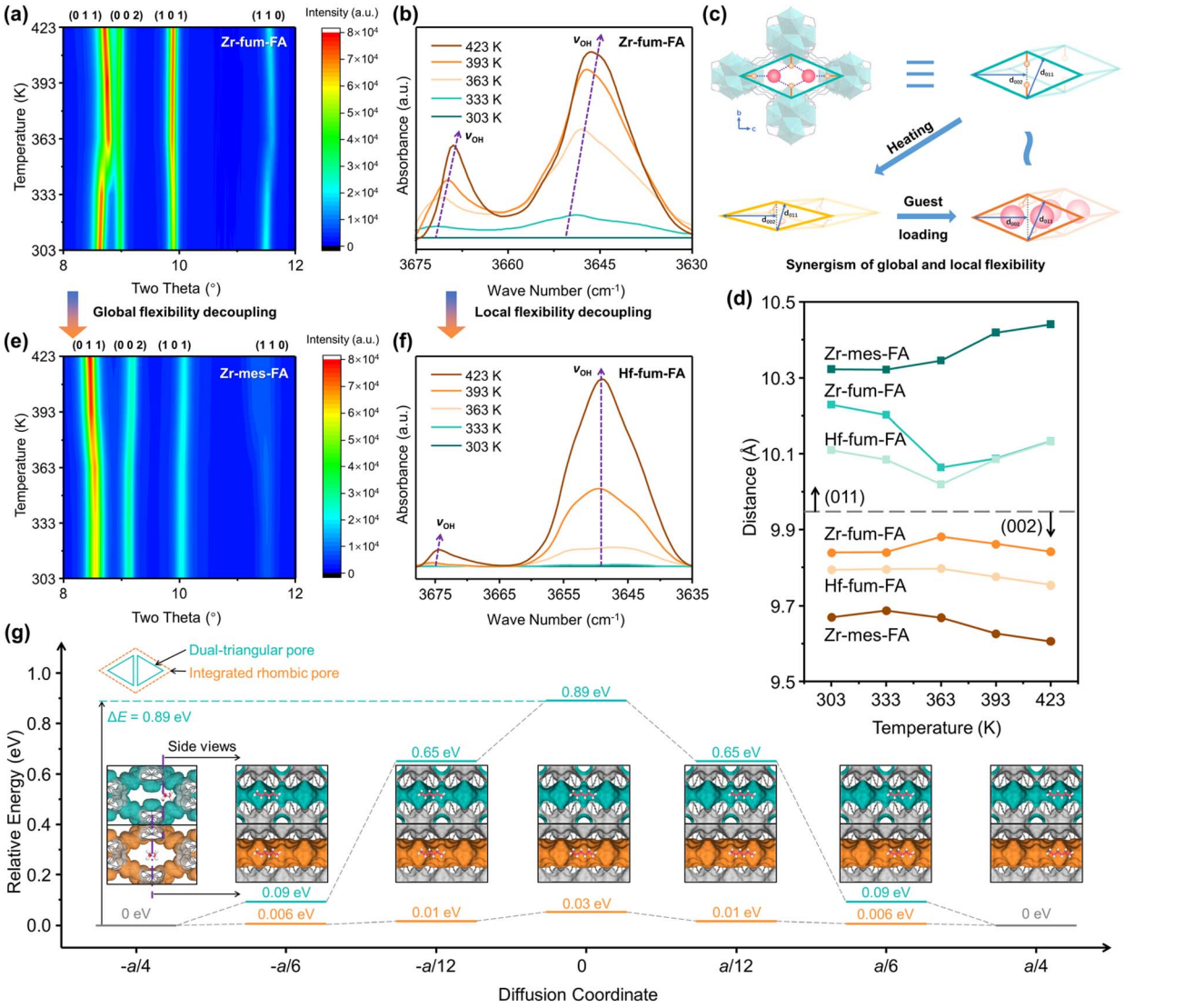

Fig. 5 Structural transformation and adsorption mechanism. (a) *In situ* PXRD patterns of Zr-fum-FA under a 3-MP saturated N_2 flow with a temperature range of 303 to 423 K. (b) DRIFTS spectra of Zr-fum-FA under N_2 flow with a temperature range of 303 to 423 K. (c) The representation of temperature- and guest-responsive structural transformation of Zr-fum-FA (the orange and pink balls represent hydroxyl groups and guest molecules, respectively), and (d) the corresponding interplanar spacing changes of (011) and (002) planes at varied temperatures. (e) *In situ* PXRD patterns of global flexibility-decoupled Zr-mes-FA under the same conditions. (f) DRIFTS spectra of local flexibility-decoupled Hf-fum-FA under the same conditions. (g) The diffusion pathways and corresponding energy barriers of *n*-Hex on the original Zr-fum-FA and the hypothetical one ignoring the pendent hydroxyl groups. The coordinate *a* denotes the cell parameter *a* of Zr-fum-FA (10.03 Å).

rather than the integrated rhombic one in Zr-fum-FA (Fig. 1b). These two situations with decoupled flexibility further highlighted the synergistic effect of global and local dynamics towards improving the hexane isomer adsorption and separation performance of the materials.

The high diffusion activation energy of hexane on the pristine dual-triangular pores of Zr-fum-FA (0.89 eV, 86 kJ mol^{-1}) was further confirmed by the DFT calculations, as shown in Fig. 5g, and Table S10.† From the side view, it is evident that the one-dimensional pores have a corrugated shape with the pendent hydroxyl groups acting as bottlenecks, resulting in significant steric hindrance. By artificially removing these hydroxyl groups to simulate an integrated rhombic pore structure at high temperatures, a flat axial section can be obtained, and the diffusion activation energy of hexane can be reduced to only 0.03 eV (2.9 kJ mol^{-1}). Although the ideal integrated flat pore structure can only be constructed hypothetically, the actual situation should be an intermediate state between the two extreme structures shown in Fig. 5g. The apparent behavior of the system was prone to be dominated by the large-pore state above 363 K and *vice versa*, as confirmed by *in situ* PXRD and DRIFTS measurements. Therefore, the reason for the two-stage deviation from the Arrhenius equation (Fig. S30†) has been successfully traced through the DFT simulation to be the partial delocalization of the pendent hydroxyl groups.

Conclusions

In summary, the sequential sieving and separation of hexane isomers with varied branching degrees have been successfully achieved on the temperature-responsive flexible Zr-fum-FA MOF. The pore structure undergoes a transformation from segmented double triangular pores at low temperatures, allowing only *n*-hexane to enter, to an integrated rhombic pore at high temperatures, enabling the separation of mono- and di-branched isomers. The dual sieving ability is attributed to the synergistic effect of the global dynamics of the framework and the local flexibility of vibration-enhanced hydroxyl groups, as demonstrated by *in situ* PXRD, DRIFTS, and DFT calculations. Furthermore, precise control and decoupling of the flexibility are achieved through two distinct strategies: incorporating damping blocks (methyl groups) within the framework to restrict its global dynamics, and substituting the metal nodes to limit the local vibration of terminal hydroxyl groups. These two situations with decoupled flexibilities further elucidated their separate and synergistic effects on the sieving performance of the materials. This study not only provides a class of robust MOFs for the efficient sieving and separation of hexane isomers, but also develops effective approaches for the rational design and regulation of temperature-responsive flexibilities in MOFs. The insights gained from this work pave the way for the development of advanced adsorbents with desired dynamic behaviors for challenging separations in the petrochemical industry and beyond.

Data availability

The data supporting this article have been included as part of the ESI.†

Author contributions

F. Zheng and Z. Bao conceived and designed the project. R. Chen and J. Li synthesized the materials, performed most of the adsorption and breakthrough experiments, and drafted the manuscript. F. Zhou performed the adsorption kinetics experiment. B. Sheng carried out the molecular simulation and analyzed the binding sites of the guests. B. Liu participated in the data discussion and writing of the manuscript. Q. Yang, Z. Zhang and Q. Ren discussed the experimental results and gave valuable suggestions. F. Zheng and Z. Bao supervised the experiment and revised the manuscript.

Conflicts of interest

There are no conflicts to declare.

Acknowledgements

We gratefully acknowledge the financial support from the National Natural Science Foundation of China (no. 22225802, 22288102, 22421004, U23A20120, 223B2803), and Zhejiang Provincial Natural Science Foundation of China (no. LZ22B060002).

Notes and references

1 R. A. Myers, *Handbook of petroleum refining processes*, McGraw-Hill, New York, 2004.
2 I. Amghizar, L. A. Vandewalle, K. M. Van Geem and G. B. Marin, *Engineering*, 2017, **3**, 171–178.
3 A. Aitani, M. N. Akhtar, S. Al-Khattaf, Y. Jin, O. Koseoglo and M. T. Klein, *Energy Fuels*, 2019, **33**, 3828–3843.
4 D. Peralta, G. Chaplais, A. Simon-Masseron, K. Barthelet and G. D. Pirngruber, *Ind. Eng. Chem. Res.*, 2012, **51**, 4692–4702.
5 F. Xie, L. Yu, H. Wang and J. Li, *Angew. Chem. Int. Ed.*, 2023, **62**, e202300722; *Angew. Chem.*, 2023, **135**, e202300722.
6 J. A. C. Silva and A. E. Rodrigues, *AIChE J.*, 1997, **43**, 2524–2534.
7 M. Eddaoudi, J. Kim, N. Rosi, D. Vodak, J. Wachter, M. O'Keeffe and O. M. Yaghi, *Science*, 2002, **295**, 469–472.
8 Z. R. Herm, B. M. Wiers, J. A. Mason, J. M. van Baten, M. R. Hudson, P. Zajdel, C. M. Brown, N. Masciocchi, R. Krishna and J. R. Long, *Science*, 2013, **340**, 960–964.
9 P.-Q. Liao, N.-Y. Huang, W.-X. Zhang, J.-P. Zhang and X.-M. Chen, *Science*, 2017, **356**, 1193–1196.
10 R.-B. Lin, L. Li, H.-L. Zhou, H. Wu, C. He, S. Li, R. Krishna, J. Li, W. Zhou and B. Chen, *Nat. Mater.*, 2018, **17**, 1128–1133.
11 H. Zeng, M. Xie, T. Wang, R.-J. Wei, X.-J. Xie, Y. Zhao, W. Lu and D. Li, *Nature*, 2021, **595**, 542–548.
12 Y. Yang, L. Li, R.-B. Lin, Y. Ye, Z. Yao, L. Yang, F. Xiang, S. Chen, Z. Zhang, S. Xiang and B. Chen, *Nat. Chem.*, 2021, **13**, 933–939.
13 K. B. Idrees, Z. Li, H. Xie, K. O. Kirlikovali, M. Kazem-Rostami, X. Wang, X. Wang, T.-Y. Tai, T. Islamoglu, J. F. Stoddart, R. Q. Snurr and O. K. Farha, *J. Am. Chem. Soc.*, 2022, **144**, 12212–12218.
14 Y. Su, K. Otake, J.-J. Zheng, S. Horike, S. Kitagawa and C. Gu, *Nature*, 2022, **611**, 289–294.
15 Z. Zheng, A. H. Alawadhi, S. Chheda, S. E. Neumann, N. Rampal, S. Liu, H. L. Nguyen, Y. Lin, Z. Rong, J. I. Siepmann, L. Gagliardi, A. Anandkumar, C. Borgs, J. T. Chayes and O. M. Yaghi, *J. Am. Chem. Soc.*, 2023, **145**, 28284–28295.
16 H. Wang, X. Dong, J. Lin, S. J. Teat, S. Jensen, J. Cure, E. V. Alexandrov, Q. Xia, K. Tan, Q. Wang, D. H. Olson, D. M. Proserpio, Y. J. Chabal, T. Thonhauser, J. Sun, Y. Han and J. Li, *Nat. Commun.*, 2018, **9**, 1745.
17 Q. Chen, S. Xian, X. Dong, Y. Liu, H. Wang, D. H. Olson, L. J. Williams, Y. Han, X.-H. Bu and J. Li, *Angew. Chem. Int. Ed.*, 2021, **60**, 10593–10597; *Angew. Chem.*, 2021, **133**, 10687–10691.
18 E. Velasco, S. Xian, H. Wang, S. Teat, D. Olson, K. Tan, S. Ullah, T. Popp, A. Bernstein, K. Oyekan, A. Nieuwkoop, T. Thonhauser and J. Li, *ACS Appl. Mater. Interfaces*, 2021, **13**, 51997–52005.
19 R. Chen, F. Zhou, B. Sheng, Z. Zhang, Q. Yang, Y. Yang, Q. Ren and Z. Bao, *ACS Sustainable Chem. Eng.*, 2022, **10**, 11330–11337.

20 B. Lal, K. B. Idrees, H. Xie, C. S. Smoljan, S. Shafaie, T. Islamoglu and O. K. Farha, *Angew. Chem. Int. Ed.*, 2023, **62**, e202219053; *Angew. Chem.*, 2023, **135**, e202219053.
21 H. Wang, X. Dong, J. Ding, K. Wang, L. Yu, S. Zhang, Y. Han, Q. Gong, A. Ma and J. Li, *Chem. Eur. J.*, 2021, **27**, 11795–11798.
22 Q. Gong, L. Yu, J. Ding, S. Zhang, Y. Bo, K. Chi, H. Wang, Q. Xia, S. He and J. Li, *Sep. Purif. Technol.*, 2022, **294**, 121219.
23 Q. Yu, L. Guo, D. Lai, Z. Zhang, Q. Yang, Y. Yang, Q. Ren and Z. Bao, *Sep. Purif. Technol.*, 2021, **268**, 118646.
24 L. Yu, X. Dong, Q. Gong, S. R. Acharya, Y. Lin, H. Wang, Y. Han, T. Thonhauser and J. Li, *J. Am. Chem. Soc.*, 2020, **142**, 6925–6929.
25 L. Yu, S. Ullah, H. Wang, Q. Xia, T. Thonhauser and J. Li, *Angew. Chem. Int. Ed.*, 2022, **61**, e202211359; *Angew. Chem.*, 2022, **134**, e202211359.
26 L. Yu, S. Ullah, K. Zhou, Q. Xia, H. Wang, S. Tu, J. Huang, H.-L. Xia, X.-Y. Liu, T. Thonhauser and J. Li, *J. Am. Chem. Soc.*, 2022, **144**, 3766–3770.
27 Z. Zhang, S. B. Peh, C. Kang, K. Yu and D. Zhao, *Angew. Chem. Int. Ed.*, 2022, **61**, e202211808; *Angew. Chem.*, 2022, **134**, e202211808.
28 Y. Su, R. Chen, P. Zhang, X. He, X. Liu, Y. Liu, H. Xiong, Z. Zhao, J. Luo, J. Chen, S. Chen, Z. Zeng, Z. Bao, S. Deng and J. Wang, *AIChE J.*, 2023, **69**, e17937.
29 F. Xie, L. Yu, T. Jenkins, J. Shutak, K. Tan, T. Thonhauser, H. Wang and J. Li, *ACS Mater. Lett.*, 2024, **6**, 43–48.
30 R. Chen, F. Zheng, J. Li, Y. Liu, F. Zhou, H. Sun, Q. Yang, Z. Zhang, Q. Ren and Z. Bao, *Small Struct.*, 2024, **5**, 2300302.
31 A. Henrique, T. Maity, H. Zhao, P. F. Brântuas, A. E. Rodrigues, F. Nouar, A. Ghoufi, G. Maurin, J. A. C. Silva and C. Serre, *J. Mater. Chem. A*, 2020, **8**, 17780–17789.
32 P. F. Brântuas, A. Henrique, M. Wahiduzzaman, A. von Wedelstedt, T. Maity, A. E. Rodrigues, F. Nouar, U.-H. Lee, K.-H. Cho, G. Maurin, J. A. C. Silva and C. Serre, *Adv. Sci.*, 2022, **9**, 2201494.
33 C. S. Smoljan, Z. Li, H. Xie, C. J. Setter, K. B. Idrees, F. A. Son, F. Formalik, S. Shafaie, T. Islamoglu, L. K. Macreadie, R. Q. Snurr and O. K. Farha, *J. Am. Chem. Soc.*, 2023, **145**, 6434–6441.
34 F.-A. Guo, J. Wang, C. Chen, X. Dong, X. Li, H. Wang, P. Guo, Y. Han and J. Li, *Angew. Chem. Int. Ed.*, 2023, **62**, e202303527; *Angew. Chem.*, 2023, **135**, e202303527.
35 K. B. Idrees, K. O. Kirlikovali, C. Setter, H. Xie, H. Brand, B. Lal, F. Sha, C. S. Smoljan, X. Wang, T. Islamoglu, L. K. Macreadie and O. K. Farha, *J. Am. Chem. Soc.*, 2023, **145**, 23433–23441.
36 A. Henrique, A. E. Rodrigues and J. A. C. Silva, *Sep. Purif. Technol.*, 2020, **238**, 116419.
37 P. A. P. Mendes, P. Horcajada, S. Rives, H. Ren, A. E. Rodrigues, T. Devic, E. Magnier, P. Trens, H. Jobic, J. Ollivier, G. Maurin, C. Serre and J. A. C. Silva, *Adv. Funct. Mater.*, 2014, **24**, 7666–7673.
38 D. Lv, H. Wang, Y. Chen, F. Xu, R. Shi, Z. Liu, X. Wang, S. J. Teat, Q. Xia, Z. Li and J. Li, *ACS Appl. Mater. Interfaces*, 2018, **10**, 6031–6038.
39 Y. Ling, Z. X. Chen, F. P. Zhai, Y. M. Zhou, L. H. Weng and D. Y. Zhao, *Chem. Commun.*, 2011, **47**, 7197–7199.
40 P. S. Barcia, F. Zapata, J. A. C. Silva, A. E. Rodrigues and B. J. Chen, *Phys. Chem. B*, 2007, **111**, 6101–6103.
41 D.-D. Zhou and J.-P. Zhang, *Acc. Chem. Res.*, 2022, **55**, 2966–2977.
42 H. Wang, X. Dong, E. Velasco, D. H. Olson, Y. Han and J. Li, *Energy Environ. Sci.*, 2018, **11**, 1226–1231.
43 Y. Lin, L. Yu, S. Ullah, X. Li, H. Wang, Q. Xia, T. Thonhauser and J. Li, *Angew. Chem. Int. Ed.*, 2022, **61**, e202214060; *Angew. Chem.*, 2022, **134**, e202214060.
44 R. Chen, L. Li, D. H. Olson, L. Guo, L. Chen, Q. Yang, Q. Xu, Z. Zhang, Q. Ren, J. Li and Z. Bao, *Small*, 2023, **19**, 2207367.
45 F. Zheng, L. Guo, R. Chen, F. Zhou, Z. Zhang, Q. Yang, Y. Yang, Q. Ren and Z. Bao, *Chem. Eng. J.*, 2023, **460**, 141743.
46 S. Wang, N. Xhaferaj, M. Wahiduzzaman, K. Oyekan, X. Li, K. Wei, B. Zheng, A. Tissot, J. Marrot, W. Shepard, C. Martineau-Corcos, Y. Filinchuk, K. Tan, G. Maurin and C. Serre, *J. Am. Chem. Soc.*, 2019, **141**, 17207–17216.
47 E. Glueckauf, *Trans. Faraday Soc.*, 1955, **51**, 1540–1551.